Synthetic ultrawideband orbital angular momentum radar

Daniel J. Orfeo,[a] **Dylan Burns**,[a] **Dryver R. Huston**,[a,*] **and Tian Xia**[b]

[a]University of Vermont, Department of Mechanical Engineering, Burlington, Vermont, United States

[b]University of Vermont, Department of Electrical and Biomedical Engineering, Burlington, Vermont, United States

Abstract. Control of orbital angular momentum (OAM) offers the potential for increases in control and sensitivity for high-performance microwave systems. EM waves with properties dependent on spatial distribution are said to be "structured." Control of OAM in microwave systems is an example of a wave structure that exploits EM degrees of freedom, which most conventional systems do not use. OAM is characterized by an integer OAM mode in which zero represents the case of a plane wave and nonzero OAM modes propagate with a helical wavefront. A uniform circular phased array approach is utilized to produce helix-shaped OAM wavefronts. This method offers a critical advantage over common fixed-frequency dielectric lenses; the phases of all antenna elements are programmable across a wide frequency range, which is necessary for ultrawideband (UWB) radar imaging. Simulations and laboratory experiments are performed to determine the requirements and capabilities of an UWB OAM radar that uses the circular phased array approach. Key results include OAM phase front characterization, detection of specified OAM modes, and configuration of a network analyzer UWB radar with synthetic OAM mode-control via signal post-processing. © *2021 Society of Photo-Optical Instrumentation Engineers (SPIE)* [DOI: 10.1117/1.JRS.15.017504]

Keywords: finite-difference time-domain; gprMax; orbital angular momentum; phased array; radar; wideband.

Paper 200690 received Sep. 20, 2020; accepted for publication Mar. 9, 2021; published online Mar. 31, 2021.

1 Orbital Angular Momentum in Microwave Systems

Ground penetrating radar (GPR) and wall penetrating radars operate by transmitting, receiving, and analyzing electromagnetic (EM) waves that interact with subsurface features in dielectric structures such as earth, concrete, and building walls. The severity of each of these interactions depends on an interplay of wavelength, polarization, antenna orientation, and spatial distribution of wave properties. EM beams with both amplitude and phase dependent on spatial distribution are said to be "structured."[1] One type of waveform structure is orbital angular momentum (OAM). Control of OAM in microwave systems is an example of a wave structure that exploits EM degrees of freedom, which most conventional systems do not use. This is of interest for improving radar detection capability for certain shaped objects.[2]

EM waves and its photons carry both linear and angular momentum. Angular momentum can be either spin angular momentum (SAM), which corresponds to polarization, or OAM. There are two types of OAM. Extrinsic OAM is analogous to mechanical angular momentum: because an EM beam carries linear momentum, $\vec{P}$, choosing a coordinate reference and a point in space yields an extrinsic OAM:

$$\vec{L}_E = \vec{r} \times \vec{P}. \tag{1}$$

*Address all correspondence to Dryver R. Huston, dryver.huston@uvm.edu

Extrinsic OAM depends on the choice of the coordinate system and corresponds to beam trajectory.[3,4] The more interesting option is intrinsic OAM, which corresponds to EM beam helicity.[4] This paper focuses on intrinsic OAM, hereafter simply, "OAM." OAM holds advantages over the conventional use of polarization. Polarization is a property of SAM that defines the orientation of the oscillations of a wave; however, it constrains antenna orientation and there are only two states of SAM.[5] In comparison, there are theoretically an infinite number of orthogonal OAM modes. An important distinction should be made between waves with OAM and waves with circular polarization—these are independent properties. Indeed, a beam of light can have both circular polarization and OAM. Longitudinal waves, such as acoustic waves, cannot be polarized, yet can carry OAM.[6,7] For transverse waves capable of polarization (such as EM waves), SAM can be converted to OAM.[8]

At the photon level, OAM appears as a quantum degree of freedom with integer quanta of angular momentum added to each photon. The objective then is to have a macroscopic interpretation in which continuous EM fields are compatible with this quantized interpretation. To do this, OAM can be represented in the macroscopic regime as paraxial EM beams with an orthogonal decomposition of Laguerre–Gaussian (LG) modes.[9] LG modes are integers, suggesting a direct link between the quantum and macroscopic interpretations: LG modes are the eigenmodes of the OAM operator.[9] The generalized Laguerre polynomials for $\alpha \in \Re$ and coefficient $n \in \mathbb{N}_1$ are the polynomial solutions of the following[10] differential equation:

$$xy'' + (\alpha + 1 - x)y' + ny = 0. \tag{2}$$

The beam profiles are solved using the LG modal decomposition. These functions are written in cylindrical coordinates using generalized Laguerre polynomials:

$$u(r,\phi,z) = C_{lp}^{LG}\frac{w_0}{w(z)}\left(\frac{r\sqrt{2}}{w(z)}\right)^{|l|}\exp\left(-\frac{r^2}{w^2(z)}\right)L_p^{|l|}\left(\frac{2r^2}{w^2(z)}\right) \times \exp\left(-ik\frac{r^2}{2R(z)}\right)\exp(-il\phi)\exp(i\psi(z)), \tag{3}$$

where C_{lp}^{LG} is a normalization constant.[9] The result is that each OAM mode has a helical wavefront geometry with an integer mode number corresponding to the handedness and number of intertwined helices,[11] for example, a single helix, double helix, etc. OAM mode number zero represents the case of a plane wave. The overall effect is helix-shaped waves[12] with a pitch length on the order of the wavelength and energy concentrated in a ring around the propagation axis, with no energy at the center along the axis. Because phase is undefined at the center of the helix, the electric field $\vec{E}$ is undefined, leading to zero field intensity.[13] This characteristic annular intensity distribution[14] is why OAM beams may also be said to have a vortex structure.

To date, many investigations of rotating-field EM beams have occurred in the optical regime,[15] and most microwave systems are unable to take advantage of the additional degrees of freedom offered by helically structured light. LG modes are mathematically mutually orthogonal and represent a theoretical means of propagating EM waves with different information content along the same beamline at the same wavelength,[12,16] increasing the rate of data transmission[17] and improving spectral efficiency. In addition, just as antenna orientation and polarization have a significant effect on signal returns for conventional penetrating microwave radars,[18] certain object shapes or arrangements may be easier to detect using a radar operating with a specific OAM mode due to potentially unique scattering properties of waveforms with OAM. Of particular interest is whether microwave beams with OAM interact with shaped subsurface features, such as congested pipes or corners, in a different manner than that of nonrotating beams.

OAM can be induced in microwaves by broadcasting a plane wave through a spiral phase plate (SPP) dielectric, which introduces an azimuthally dependent phase delay,[19,20] as shown in Fig. 1(a). However, SPPs are frequency-specific, which presents an obstacle for harnessing OAM in frequency-modulated communication systems and wide-bandwidth radar. Complex phase fronts such as the OAM helix can be produced using a coherent array of antenna emitters,

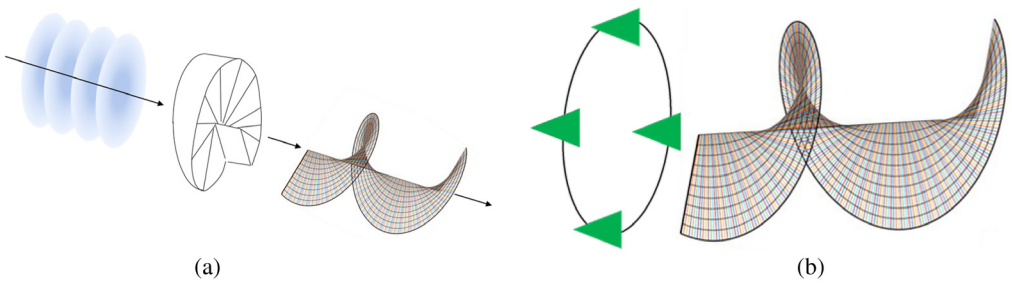

Fig. 1 (a) OAM is induced by broadcasting a plane wave through a spiral phase plate (SPP) dielectric, which introduces an azimuthally dependent phase delay. (b) An OAM + 1 (left-handed) EM wave propagating from a four-antenna circular phased array of microwave antennas.

each of which can be phase controlled to create a beam.[21] Figure 1(b) shows a circular phased array that generates the desired helical wavefront.[21,22] This approach offers a critical advantage: the phases of all antenna elements are programmable across different frequencies. As a result, transmission and reception of an OAM beam can be controlled across a wide frequency bandwidth.

2 Phase Front of the OAM Waveform

A uniform circular phased array can be configured with different numbers of antenna elements. Because this may impact the structure and quality of the generated OAM waveform, it is useful to characterize the phase front created by a given circular phased array. In this experiment, frequency $f = 1$ GHz, radius $a = \lambda$, and OAM mode $l = +1$. These values were chosen to be realistic for a GPR application and for comparison with work published by Mohammadi et al.[23,24] and Liu et al.[25] To calculate a phase front, Maxwell's equations are written in a potential formulation where $\mathbf{A}$ is the magnetic vector potential and thereby the curl of $\mathbf{A}$ is the magnetic field $\mathbf{B}$: $\nabla \times \mathbf{A} = \mathbf{B}$. The advantage of this formulation is that it is convenient to visually identify the EM geometry of a phase front by taking the phase angle of $\mathbf{A}$ at every point in a plane of interest.

When the number of antennas (N) is sufficiently large, a circular antenna array can be idealized as a continuous circular emitter:[23,25]

$$\mathbf{A}(\mathbf{r}) \sim \frac{e^{ikr}}{r} i^{-l} e^{il\varphi} J_l(ka \sin \theta), \tag{4}$$

where a is the radius of the circular phased array, J_l is a Bessel function of the first kind, k is the wave vector magnitude λ^{-1}, l is the OAM mode number, and φ is the azimuth angle. MATLAB provided a numerical evaluation of this expression for the given parameters. Figure 2(d) shows the characteristic spiral-shaped phase front of $\mathbf{A}$ generated by the continuous circular emitter shown in Fig. 2(a). For the three phase fronts shown in Fig. 2, the view is a slice perpendicular to the propagation axis, shown at 1.5 m in front of the array. The visible window of the slice has dimensions 3.2 m by 3.2 m, and phase is shown from $-\pi$ (blue) to π (red).

The continuous emitter assumption may not always be applicable, however. Gigahertz-frequency microwave antennas have nontrivial physical dimensions that limit the number of antenna elements that can be placed in a circular phased array. Furthermore, high-quality multichannel microwave equipment is often expensive, which places practical limits on the number of antennas used in many research applications. Because of this, a discrete model that can model the vector potential created by a relatively small number of phased array antenna elements is considered. The vector potential ($\mathbf{A}$) for a circular array of N antennas[23,25] is expressed as

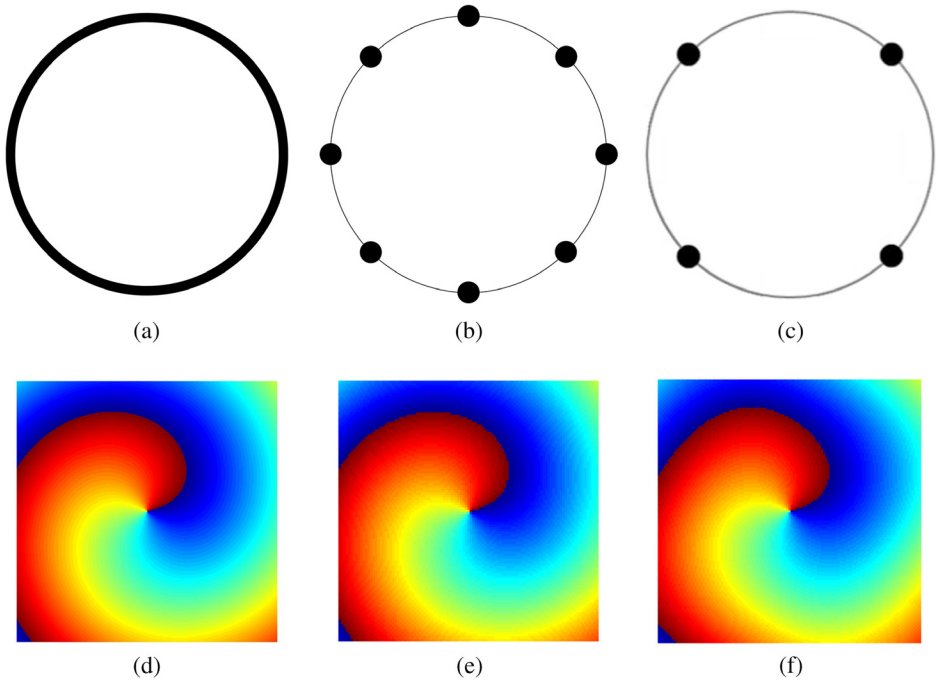

Fig. 2 Phase fronts of A with the parameters: frequency $f = 1$ GHz, radius $a = \lambda$, and OAM mode $l = +1$. The view is a slice perpendicular to the propagation axis, shown at 1.5 m in front of the array, and the visible window of the slice has dimensions 3.2 m by 3.2 m. (a) Continuous circular emitter. (b) Circular phased array with $N = 8$ antennas. (c) Circular phased array with $N = 4$ antennas. (d) Phase front of A for the continuous emitter. (e) Phase front of A for $N = 8$ antennas. (f) Phase front of A for $N = 4$ antennas.

$$\mathbf{A}(\mathbf{r}) \sim \frac{e^{ikr}}{r} \sum_{n=1}^{N} e^{-i\left(ka\left[\cos\frac{2\pi n}{N}(-x)+\sin\frac{2\pi n}{N}(-y)\right]-\frac{2\pi nl}{N}\right)}. \tag{5}$$

A phased array with many individual antenna elements ($N \to \infty$) should closely approximate the continuum case and produce a high-quality waveform. But what about an array with relatively few antennas? A circular antenna array with $N = 8$ antenna elements is shown in Fig. 2(b). Figure 2(e) shows that the phase front of **A** produced by this 8-antenna array is well-resolved and virtually indistinguishable from the continuum result in Fig. 2(d).

A more extreme four-antenna array is shown in Fig. 2(c). The phase front of **A** generated by this array is shown in Fig. 2(f). Despite some squaring-off of the spiral, the phase front shown in Fig. 2(f) exhibits the same overall structure as the continuous emitter and eight-antenna results. While this does not guarantee that it is possible to generate an OAM + 1 mode with only four antennas, it does provide evidence that low-antenna-count arrays may be practically useful for transmitting microwaves with OAM mode ± 1 characteristics. These results motivate array parameter choices for OAM experiments in the subseequent sections of this inquiry.

3 Modeling OAM with the Finite-Difference Time-Domain Method

Feynman noted that, because the three-dimensional wave equation is linear, the most general solution "is a superposition of all sorts of plane waves moving in all sorts of directions."[26] This implies that EM waves, including those with OAM, are subject to superposition in free space[5,27]—an important observation that can be leveraged to demodulate and identify OAM modes. To do this, finite-difference time-domain simulations of OAM waveforms are performed using the program gprMax.[28] Figure 3 shows the simulation configuration: an eight-element transmitter array and eight-element receiver array with radii of 1-wavelength (at 1 GHz) placed

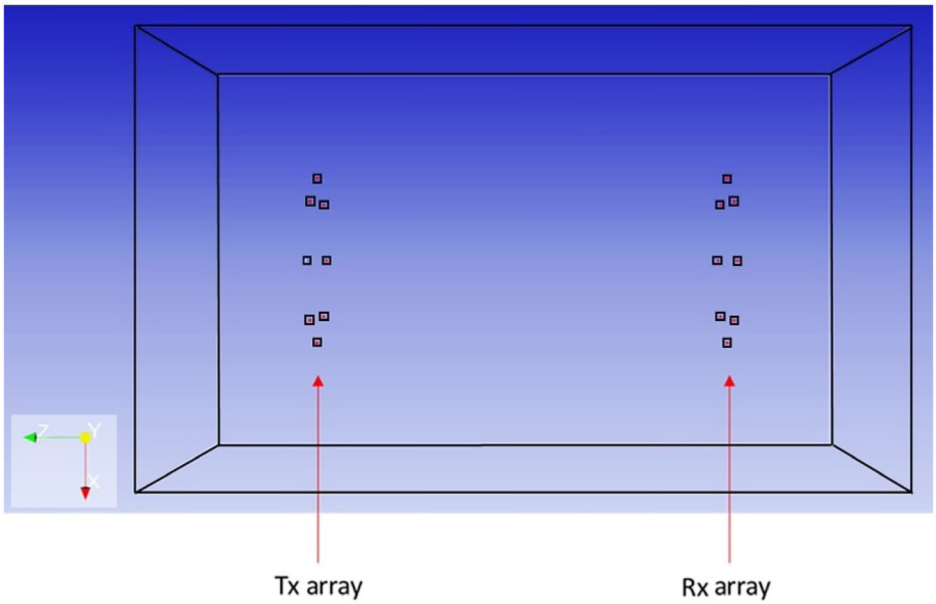

Fig. 3 (Left) An eight-element transmitter array and (right) eight-element receiver array with diameters of two wavelengths (at 1 GHz).

1.5 m apart. Simulation parameters for this model match the eight-element phased array considered in Figs. 2(b) and 2(e). Each antenna in the transmitting array broadcasts a phase-adjustable 1-GHz sine wave. The simulation domain is $1.5 \times 1.5 \times 2.5$ m, including a 0.25-m thick perfectly matched layer absorbing boundary c/ondition within each face. This domain is filled with air using the predefined gprMax material "free_space" (relative permittivity $\epsilon_r = 1$, conductivity $\sigma = 0$ Siemens/meter, and index of refraction $n = 1$). The time step is 6.16 ps with a 9.9 ns simulation duration. The spatial resolution in the X, Y, and Z directions is 3.2 mm. To verify model-function, a single sine wave is simulated. This sine wave is transmitted from one Y-direction polarized antenna in the transmitter array, and X, Y, and Z components of this waveform are received at each of the eight receiver antennas. The Y-direction components are selected, and a moving-mean filter is applied to each of the received signals to remove high-frequency noise. These data are plotted in Fig. 4(a). Due to geometric path lengths between antenna elements, three pairs of signals overlap exactly. Because of this, five sine waves are visible in the plot.

To simulate waveforms with different OAM modes, sine waves are transmitted from all eight antennas in the transmitter array and received by all eight antennas in the receiver array. The received Y-component signals are smoothed by a moving-mean filter and plotted as before. In Fig. 4(b), all eight sine waves are transmitted with the same phase, to produce an OAM 0 (plane wave) waveform. Due to the path lengths, all eight signals overlap almost exactly. Figures 4(c) and 4(d) show that OAM modes with opposite signs result in opposite received signal orders. Figure 4(c) shows sine waves transmitted with phase delays to produce an OAM -1 (right-handed single helix) waveform. Right-handedness is shown by the signal order, from left to right in the plot: Rx1, Rx2, Rx3, Rx4, Rx5, Rx6, Rx7, Rx8. In Fig. 4(d), sine waves are transmitted with phase delays to produce an OAM +1 (left-handed single helix) waveform. Left-handedness is shown by the signal order, from left to right: Rx8, Rx7, Rx6, Rx5, Rx4, Rx3, Rx2, Rx1. Therefore, the left-to-right order of the received signals allows for discrimination of OAM mode 0, OAM mode -1, and OAM mode $+1$.

Digital OAM phase demodulation leverages superposition to identify specific OAM modes. Because a given OAM mode has a known spatially dependent phase front, these phase delays can be canceled out automatically in postprocessing. For an OAM mode $\mathbf{O}_\ell$, and a mode-specific demodulate process $\mathbf{D}_\ell$, a coherent signal $\mathbf{S}$ is obtained:

$$\mathbf{D}_\ell(\mathbf{O}_\ell) = \mathbf{S}. \tag{6}$$

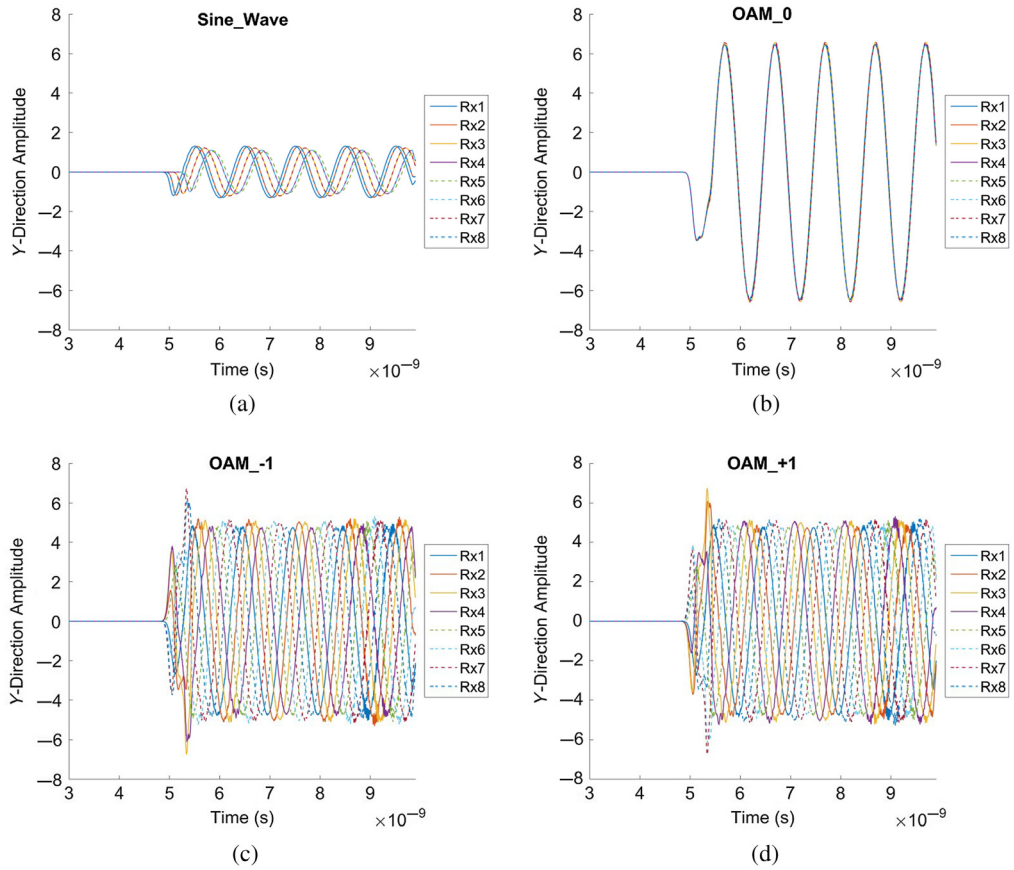

Fig. 4 (a) A single sine wave is transmitted from Tx1 in the transmitter array and received by all eight antennas in the receiver array. (b) In-phase sine waves are transmitted from all eight antennas in the transmitter array and received by all eight antennas in the receiver array (OAM 0). (c) Eight sine waves are transmitted with phase delays to produce an OAM − 1 (right-handed single helix) waveform. (d) Eight sine waves are transmitted with phase delays to produce an OAM + 1 (left-handed single helix) waveform.

If, by this method, the individual received signals demodulate into a single coherent sine wave, an OAM mode is positively identified. If the received signals remain offset, then either a different OAM mode is present or no OAM mode is present. Figure 5(a) shows OAM mode -1 demodulation applied to an OAM mode -1 waveform. After a cycle of incoherence, the waveform demodulates into a demodulated sine wave signal. Figure 5(b) shows this same OAM -1 waveform with OAM mode $+1$ demodulation applied: there is no demodulation in this case. Because OAM mode $+1$ is not present in the transmitted signal, OAM mode $+1$ demodulation does not produce a coherent waveform. Figure 5(c) shows the similar case in which OAM mode -1 demodulation fails to demodulate an OAM $+1$ waveform. Finally, Fig. 5(d) shows an OAM mode $+1$ waveform demodulated into a sine wave using OAM mode $+1$ processing. Not only does this result validate OAM modal identification by demodulation, but it also demonstrates a way in which superposition can be exploited in free-space OAM experiments. The following section takes this further, exploiting EM superposition to conduct OAM experiments in the frequency domain.

4 Synthetic Ultrawideband OAM with a Network Analyzer

4.1 *System Overview*

A radar that operates over a wide frequency bandwidth can deliver high-resolution imaging. However, most current OAM systems operate at only a single or narrow frequency band.

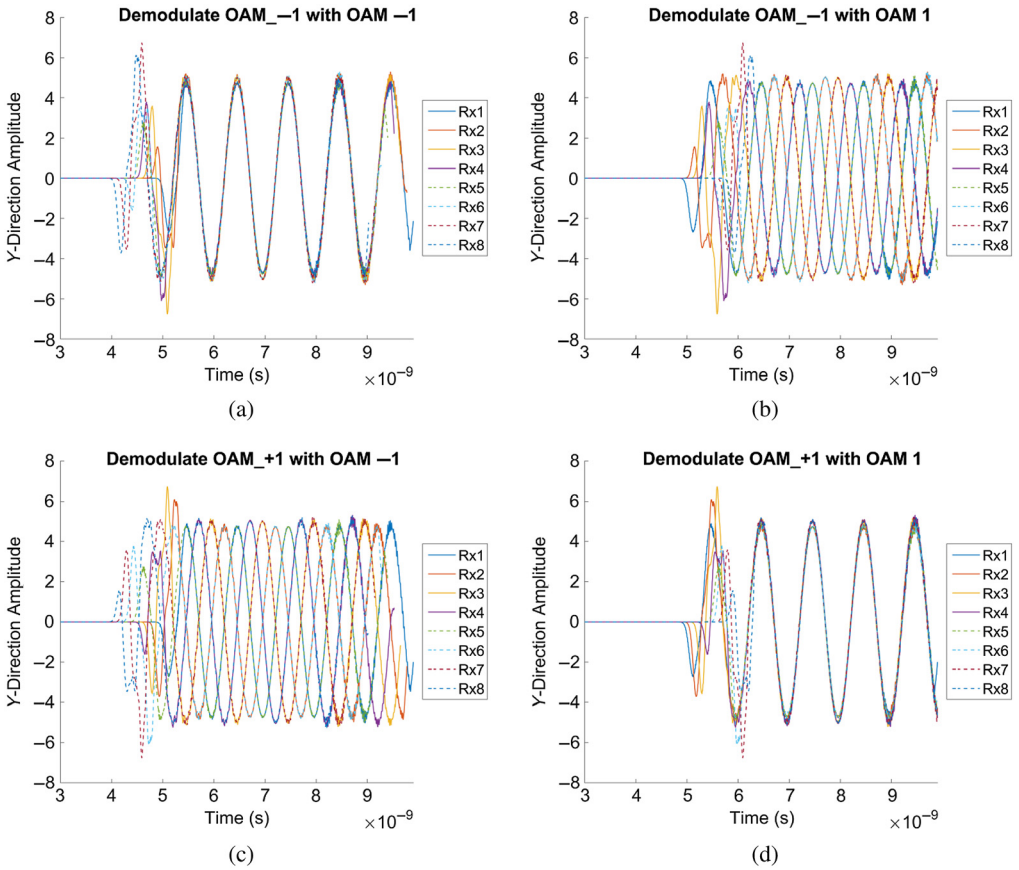

Fig. 5 (a) Transmit mode −1 and demodulate with mode −1. (b) Transmit mode −1 and demodulate with mode +1. (c) Transmit mode +1 and demodulate with mode −1. (d) Transmit mode +1 and demodulate with mode +1.

In this section, an ultrawideband (UWB) OAM radar based on a network analyzer is proposed. This system allows for OAM measurements to be conducted natively at frequencies of interest during a frequency sweep. The process leverages superposition and postprocessing to recreate synthetically the behavior of an OAM waveform. Individual magnitude and phase measurements are combined to synthesize OAM waveforms that have the same properties as those generated by a simultaneously transmitting phased array. To verify the performance of this system, spiral reflectors are used to detect a specific OAM mode at a specific frequency. The operational frequency range of a network analyzer gives this OAM system UWB capability, a unique innovation for an OAM radar.

The operating theory behind the function of synthetic OAM is the implementation of a fractional Hilbert transform (FHT).[29] The conventional Hilbert transform (HT) imparts a ±90- deg phase shift to every frequency component of a complex signal via multiplication by $\mathbf{i}$. This gives positive frequencies a shift of +90 deg and negative frequencies a shift of −90 deg. For a pure sine or cosine,[30]

$$H[\sin\,\omega t] = \frac{1}{\pi}\int_{-\infty}^{\infty}\frac{\sin\,\omega\tau}{\tau - t}\mathrm{d}\tau = \cos\,\omega\tau \quad \omega > 0, \tag{7}$$

$$H[\cos\,\omega t] = \frac{1}{\pi}\int_{-\infty}^{\infty}\frac{\cos\,\omega\tau}{\tau - t}\mathrm{d}\tau = -\sin\,\omega\tau \quad \omega > 0. \tag{8}$$

An FHT, by contrast, can impart an arbitrary designated phase shift.[31] The FHT has been used in signal processing[32] for tasks such as image edge enhancement and image compression.[33] For this research, the ability to designate a specific user-defined phase shift is critical for

implementing the phase delays necessary to produce a coherent OAM mode from a circular phased array. The FHT is defined in the frequency domain as[29]

$$\mathcal{H}_{\alpha}(f) = [\cos\,\varphi + i * \mathrm{sgn}(f) * \sin\,\varphi][X_R(f) + i * X_I(f)], \tag{9}$$

where φ is the phase of the FHT, $\mathrm{sgn}(f)$ is the signum function, and $X_R(f)$ and $X_I(f)$ are the real and imaginary parts of the Fourier transform of the original signal, respectively. In reality, implementation is very straightforward because the network analyzer operates natively in the frequency domain and gives the operator individual measurements of magnitude and phase for each frequency component. Therefore, implementation of an FHT is as simple as inserting the desired phase shifts directly into the individual frequency components. An inverse Fourier transform can then be used to recover a time-domain response if radar imaging is desired.

4.2 *Equipment Configuration*

A four-channel Keysight PNA-X N5241A network analyzer with UWB frequency-domain operation from 10 MHz to 13.5 GHz was chosen for this experiment; see Fig. 6. For each pair-combination of the four antennas in a circular transceiver array, magnitude and phase data are recorded for frequencies from 10 MHz to 13.5 GHz. This gives 16 antenna-pair measurement combinations of magnitude and phase at each sampled frequency: $S_{11}, S_{12} \ldots S_{43}, S_{44}$. In particular, S_{11}, S_{22}, S_{33}, S_{44} represent perpendicular reflections in which a signal is transmitted, reflected from a target, and then received by the same antenna. This gives interpretable information about the phase distribution of the spatially structured OAM waveform. However, due to the hardware functionality of a network analyzer, simultaneous transmission and reception of multiple channel combinations are not possible, and phase delays are not set on the transmission side. This means that a true OAM waveform cannot be created. Instead, individual measurements are taken one at a time, and helical OAM phasing is introduced automatically in postprocessing. In the previous section, OAM demodulation was used to show that superposition is valid in free space; therefore, it should be possible to extract useful information from these individual measurements, provided complete (i.e., complex) magnitude and phase information is present. Leveraging superposition in this manner via postprocessing gives synthetic OAM capabilities.

4.3 *Determining the Properties of Synthetic OAM*

A test was devised to determine if the synthetic OAM waveforms exhibit the same scattering characteristics as OAM waveforms produced by a simultaneously transmitting phased array. The idea is to detect nonzero OAM modes with a spiral reflector.[34] If the synthesized OAM waveform behaves like a true simultaneous OAM waveform, a spiral reflector will alter the phases of the reflected signals in a specific way. Then, if phase delays for the correct OAM mode are implemented in postprocessing, the received signal will be demodulated into a plane wave (OAM mode 0). For example, Fig. 6 shows a right-handed (OAM $-$ 1) reflector demodulating a left-handed (OAM $+$ 1) waveform.[22] In this case the right-handed spiral reflector subtracts OAM from the incident signal. The spiral reflector is chosen with a pitch that is half that of the incident OAM helix, to account for the round-trip path of a reflected signal. Demodulation is advantageous in this situation because S_{11}, S_{22}, S_{33}, and S_{44} measurements of plane wave signals can be summed to enhance signal-to-noise of the target. An increase in combined signal strength therefore provides confirmation of a particular OAM mode present in the incident (transmitted) signal. It is important to note that, similar to an SPP, a spiral target must be tuned to a specific frequency. Because of this, $S_{11} + S_{22} + S_{33} + S_{44}$ signal strength will only increase at or around the frequency for which the spiral reflector is tuned, even when a wide bandwidth OAM frequency sweep is performed. However, there is no reason for OAM to occur only at an arbitrarily chosen frequency, so detecting OAM characteristics at one frequency provides evidence that these characteristics will persist at the other frequencies within the frequency sweep. In this way, this test is used to determine whether or not the synthetic OAM waveform exhibits true OAM behavior. A successful test would indicate that the properties of an OAM signal can be

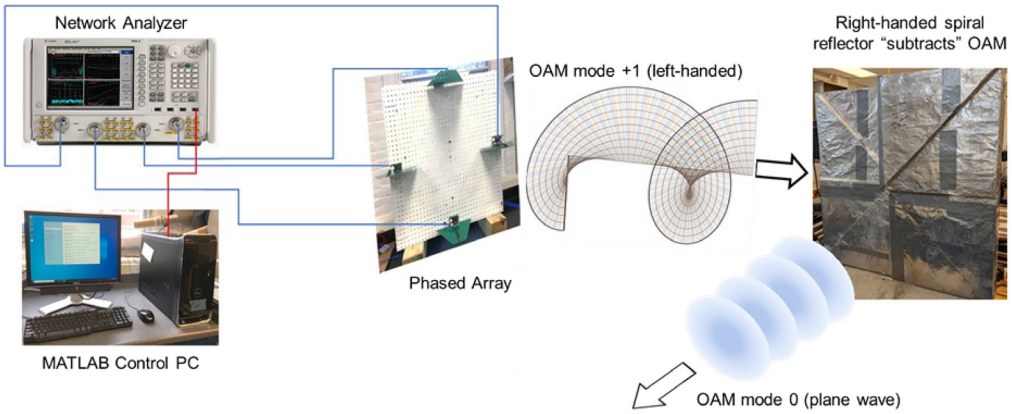

Fig. 6 The synthetic UWB OAM radar broadcasts an OAM + 1 (left-handed) waveform from a four-antenna circular transceiver array. An OAM – 1 (right-handed) spiral reflector, made from aluminum-covered foam wedges, demodulates the left-handed single helix waveform into a plane wave (OAM mode 0) for detection.

reproduced by synthetically combining individual magnitude and phase measurements. If true, a network analyzer could be used as a wide bandwidth OAM radar by leveraging superposition.

4.4 *Laboratory Test of Synthetic OAM Radar*

In this laboratory test, left- and right-handed spiral reflector targets are tuned for an incident waveform frequency of ∼1.2 GHz. Each target is designed to demodulate a specific OAM mode (−1 or +1) at 1.2 GHz. Adding the phase delays for the corresponding OAM mode will lead to OAM demodulation and increase the signal magnitude around 1.2 GHz when measuring the sum of the $S_{11} + S_{22} + S_{33} + S_{44}$ signals. Adding improper phase delays (or no phase delays) will fail to demodulate the OAM waveform and lead to a degradation of the $S_{11} + S_{22} + S_{33} + S_{44}$ signal magnitude. We therefore expect a higher signal magnitude around 1.2 GHz: for the

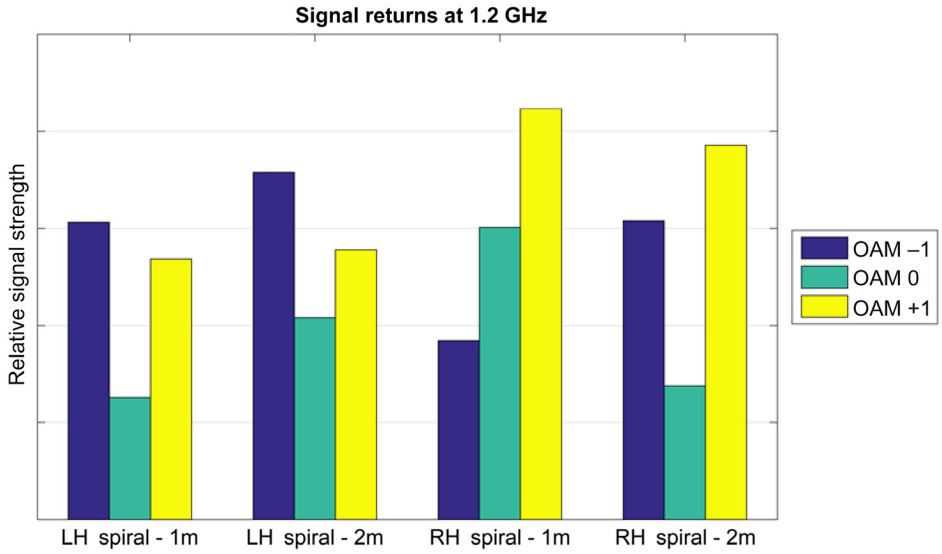

Fig. 7 $S_{11} + S_{22} + S_{33} + S_{44}$ signal magnitude when reflected from two spiral reflector targets, using three different synthetic OAM postprocessing modes. The bar chart shows the results for incident signals of 1.2 GHz, the frequency for which the spiral reflectors are tuned. Signal returns from the left-handed spiral target (at both 1-m and 2-m distances) are greatest when the incident signal is postprocessed with OAM – 1 phasing. Signal returns from the right-handed spiral target (at both 1-m and 2-m distances) are greatest when the incident signal is postprocessed with OAM + 1 phasing.

left-handed (OAM + 1) target when the incident signal is postprocessed with OAM − 1 phasing and for the right-handed (OAM − 1) target when the incident signal is postprocessed with OAM + 1 phasing. An air-shot background subtraction is performed for each trial. Figure 7 shows the results for this test. As predicted, signal returns from the left-handed spiral target are greatest when the incident signal is postprocessed with OAM − 1 phasing. OAM − 1 phasing improved signal returns by at least 13% at the 1-m distance and 25% at the 2-m distance. In a similar fashion, signal returns from the right-handed spiral target (at both 1-m and 2-m distances) are greatest when the incident signal is postprocessed with OAM + 1 phasing. Improvements here were at least 33% at 1 m and at least 22% at 2 m. This indicates successful functioning of a synthetic OAM system based on measurement superposition.

5 Summary of Results

The results of this inquiry are summarized as follows. The phase front of the vector potential ($\mathbf{A}$) of an OAM waveform can be realistically generated using a circular phased array with as few as four discrete antenna elements. This provides motivation for performing microwave simulations and laboratory tests using circular phased arrays with four to eight elements. An eight-element circular phased array is then used in a simulation model to generate waveforms with nonzero OAM. In this simulation, gigahertz-frequency OAM modes $(-1, 0, +1)$ can be received and demodulated, demonstrating superposition. Finally, a laboratory experiment that leverages superposition to validate the function of a synthetic UWB OAM radar based on a network analyzer is presented. It is found that combining individual magnitude and phase measurements can reproduce the behavior of OAM waveforms generated by a conventional simultaneously transmitting phased array. This indicates that a synthetic network analyzer system may be a viable path forward for the further development of an UWB OAM radar.

6 Discussion

The overarching goal of this research is to harness OAM for use in UWB GPR systems. Results indicate that synthetic OAM may be a viable means for achieving UWB OAM, which could provide improved detection of targets with spiral scattering cross-sections, as well as improved GPR sensitivity. This inquiry considers free-space experiments; it will be of considerable interest to evaluate the functionality of the synthetic UWB OAM system in penetrating radar applications. Additional applications may include ghost imaging via differential signal analysis between a helical OAM mode and a plane wave without OAM characteristics. The authors are currently exploring the viability of exploiting OAM waveforms for use in a counter-stealth microwave radar, as well as in land mine detection applications. Future work will focus on wideband and dual-function sensing and communication systems[35] that leverage the unique modulation and scattering potential of OAM waveforms.

Acknowledgments

This work was supported by Defense University Research Instrumentation Program (DURIP) U.S. Army Contract No. W911NF1810193, U.S. Army contract W909MY-17-C-0020 with White River Technologies, Inc., U.S. National Science Foundation Grant Nos. 1647095 and 1640687, University of Vermont SPARK Fund, University of Vermont Office for the Vice President for Research, and the Vermont Space Grant Consortium under NASA Cooperative Agreement NNX15AP86H. Portions of this work have previously been published in conference proceedings papers.[36–38] The authors declare that this research was conducted in the absence of any business or financial relationships that could be construed as a conflict of interest.

References

1. V. E. Lembessis, *Taming Atoms: The Renaissance of Atomic Physics*, pp. 43–54, SPIE Press, Bellingham, Washington (2020).

2. E. Cartier, "NASA fellowship activity 2018 (NNH18ZHA003N)," National Aeronautics and Space Administration (2018).
3. K. Y. Bliokh and F. Nori, "Transverse and longitudinal angular momenta of light," *Phys. Rep.* **592**, 1–38 (2015).
4. K. Y. Bliokh et al., "Spin–orbit interactions of light," *Nat. Photonics* **9**(12), 796–808 (2015).
5. L. Gong et al., "Optical orbital-angular-momentum-multiplexed data transmission under high scattering," *Light Sci. Appl.* **8**(1), 27 (2019).
6. B. W. Drinkwater, "An acoustic black hole," *Nat. Phys.* **16**(10), 1010–1011 (2020).
7. M. Cromb et al., "Amplification of waves from a rotating body," *Nat. Phys.* **16**(10), 1069–1073 (2020).
8. R. C. Devlin et al., "Arbitrary spin-to-orbital angular momentum conversion of light," *Science* **358**(6365), 896 (2017).
9. L. Allen et al., "Orbital angular momentum of light and transformation of Laguerre Gaussian laser modes," *Phys. Rev. A* **45**, 8185–8189 (1992).
10. M. Abramowitz and I. A. Stegun, *Handbook of Mathematical Functions with Formulas, Graphs, and Mathematical Tables*, Applied Mathematics Series, Dover Publications, Washington D.C. (1983).
11. T. Yuan et al., "Electromagnetic vortex-based radar imaging using a single receiving antenna: theory and experimental results," *Sensors* **17**(3), 630 (2017).
12. L. Cheng, W. Hong, and Z.-C. Hao, "Generation of electromagnetic waves with arbitrary orbital angular momentum modes," *Sci. Rep.* **4**, 4814 (2014).
13. P. J. Schemmel, *Vortex Radiometry: Fundamental Concepts*, p. 16, Glenn Research Center, Cleveland, Ohio (2019).
14. J. Leach et al., "Measuring the orbital angular momentum of a single photon," *Phys. Rev. Lett.* **88**(25 Pt 1), 257901 (2002).
15. A. M. Yao and M. J. Padgett, "Orbital angular momentum: origins, behavior and applications," *Adv. Opt. Photonics* **3**(2), 161–204 (2011).
16. H. Ren et al., "On-chip noninterference angular momentum multiplexing of broadband light," *Science* **352**(6287), 805 (2016).
17. NASA, "NASA Space Technology Research Fellowship (NSTRF19)," in NASA Technology Area 5.2.1, Spectrum-Efficient Technologies, NASA (2019).
18. D. Orfeo et al., "Bistatic antenna configurations for air-launched ground penetrating radar," *J. Appl. Remote Sens.* **13**(2), 027501 (2019).
19. M. Pu et al., "Catenary optics for achromatic generation of perfect optical angular momentum," *Sci. Adv.* **1**(9), e1500396 (2015).
20. R. Steiger, S. Bernet, and M. Ritsch-Marte, "Mapping of phase singularities with spiral phase contrast microscopy," *Opt. Express* **21**(14), 16282–16289 (2013).
21. B. Thidé et al., "Utilization of photon orbital angular momentum in the low-frequency radio domain," *Phys. Rev. Lett.* **99**(8), 087701 (2007).
22. M. Ibrahimi, "How do I generate OAM waves using MATLAB?" 2017, https://www.quora.com/How-do-I-generate-OAM-waves-using-MATLAB (cited 2019).
23. S. M. Mohammadi et al., "Orbital angular momentum in radio—a system study," *IEEE Trans. Antennas Propag.* **58**(2), 565–572 (2010).
24. S. M. Mohammadi et al., "Orbital angular momentum in radio: measurement methods," *Radio Sci.* **45**(4), 1–14 (2010).
25. K. Liu et al., "Orbital-angular-momentum-based electromagnetic vortex imaging," *IEEE Antennas Wireless Propag. Lett.* **14**, 711–714 (2015).
26. M. Sands, R. Feynman, and R. B. Leighton, *The Feynman Lectures on Physics: Mainly Electromagnetism and Matter*, Vol. **2**, pp. 1963–1965, Hachette Book Group, New York (1974).
27. G. Berkhout et al., "Measuring orbital angular momentum superpositions of light by mode transformation," *Opt. Lett.* **36**, 1863–1865 (2011).
28. C. Warren, A. Giannopoulos, and I. Giannakis, "gprMax: open source software to simulate electromagnetic wave propagation for ground penetrating radar," *Comput. Phys. Commun.* **209**, 163–170 (2016).

29. A. W. Lohmann, D. Mendlovic, and Z. Zalevsky, "Fractional Hilbert transform," *Opt. Lett.* **21**(4), 281–283 (1996).
30. D. Huston, *Structural Sensing, Health Monitoring, and Performance Evaluation*, Series in Sensors, B. Jones and W. B. Spillman, Eds., p. 645, Taylor and Francis, Burlington (2011).
31. K. Chaudhury and M. Unser, "The fractional Hilbert transform and dual-tree Gabor-like wavelet analysis," in *IEEE Int. Conf. Acoust., Speech and Signal Process.*, pp. 3205–3208 (2009).
32. A. Zayed, "Hilbert transform associated with the fractional Fourier transform," *IEEE Signal Process. Lett.* **5**, 206–208 (1998).
33. R. Tao, X.-M. Li, and Y. Wang, "Generalization of the fractional Hilbert transform," *IEEE Signal Process. Lett.* **15**, 365–368 (2008).
34. F. Tamburini et al., "Experimental verification of photon angular momentum and vorticity with radio techniques," *Appl. Phys. Lett.* **99**(20), 204102 (2011).
35. A. Hassanien et al., "Dual-function radar communication systems: a solution to the spectrum congestion problem," *IEEE Signal Process. Mag.* **36**(5), 115–126 (2019).
36. D. Orfeo et al., "Electrically controlled phased array OAM radar," *Proc. SPIE* **11408**, 1140810 (2020).
37. D. Orfeo et al., "Phased array for control of orbital angular momentum in microwave systems," in *IEEE Int. Symp. Phased Array Syst. and Technol.* (2019).
38. D. Orfeo et al., "Orbital angular momentum assisted ground penetrating radars," *Proc. SPIE* **11012**, 110121C (2019).

Daniel J. Orfeo is a doctoral candidate in mechanical engineering at the University of Vermont (UVM). He received his MS degree in mechanical engineering from UVM in 2018, his BS degree in mathematics and a minor in physics from UVM in 2014. A two-time Vermont Space Grant Consortium & NASA EPSCoR Fellow, his research interests include microwave and magnetic sensing and communications.

Dylan Burns is a lecturer in the Department of Mechanical Engineering at the University of Vermont (UVM). He received his BS, MS, and PhD degrees in mechanical engineering from the UVM in 2002, 2006, and 2011, respectively. His research interests include ground penetrating radar, mapping and monitoring underground utilities, laboratory product testing, and test fixture design.

Dryver R. Huston received his BS degree from the University of Pennsylvania, Philadelphia, Pennsylvania, USA, and his MA and PhD degrees from Princeton University, Princeton, New Jersey, USA, in 1983 and 1986, respectively. Since 1987, he has been a faculty member with the University of Vermont, Burlington, Vermont, USA. He has authored the book, *Structural Sensing, Health Monitoring, and Performance Evaluation*.

Tian Xia received his BE degree in electrical engineering from Huazhong University of Science and Technology, Wuhan, China, in 1994, his MS degree from Nanjing University of Posts and Telecommunications, Nanjing, China, in 2000, and his PhD in electrical and computer engineering from the University of Rhode Island, Kingston, Rhode Island, USA, in 2003. He is a professor of electrical engineering, the university of Vermont, Burlington, Vermont, USA. His research interests include sensor circuit design and signal processing.